5646–5657 *Nucleic Acids Research, 2007, Vol. 35, No. 17*
doi:10.1093/nar/gkm629

Real-time assembly and disassembly of human RAD51 filaments on individual DNA molecules

Thijn van der Heijden[1], Ralf Seidel[1], Mauro Modesti[2], Roland Kanaar[2,3], Claire Wyman[2,3],* and Cees Dekker[1,]*

[1]Kavli Institute of Nanoscience, Delft University of Technology, Lorentzweg 1, 2628 CJ Delft, [2]Department of Cell Biology and Genetics and [3]Department of Radiation Oncology, Erasmus Medical Center, 3000 CA Rotterdam, The Netherlands

Received May 16, 2007; Revised July 24, 2007; Accepted July 31, 2007

ABSTRACT

The human DNA repair protein RAD51 is the crucial component of helical nucleoprotein filaments that drive homologous recombination. The molecular mechanistic details of how this structure facilitates the requisite DNA strand rearrangements are not known but must involve dynamic interactions between RAD51 and DNA. Here, we report the real-time kinetics of human RAD51 filament assembly and disassembly on individual molecules of both single- and double-stranded DNA, as measured using magnetic tweezers. The relative rates of nucleation and filament extension are such that the observed filament formation consists of multiple nucleation events that are in competition with each other. For varying concentration of RAD51, a Hill coefficient of 4.3 ± 0.5 is obtained for both nucleation and filament extension, indicating binding to dsDNA with a binding unit consisting of multiple (≥4) RAD51 monomers. We report Monte Carlo simulations that fit the (dis)assembly data very well. The results show that, surprisingly, human RAD51 does not form long continuous filaments on DNA. Instead each nucleoprotein filament consists of a string of many small filament patches that are only a few tens of monomers long. The high flexibility and dynamic nature of this arrangement is likely to facilitate strand exchange.

INTRODUCTION

Recombination between homologous DNA molecules is a key element of proper genome maintenance and duplication. Homologous recombination is an important pathway for accurate repair of DNA double-strand breaks, is required for generating genetic diversity during meiosis, and is essential for overcoming difficulties in replication. The core mechanistic steps of homologous recombination consist of joint molecule formation and strand exchange between DNA molecules. In homologous recombination, one DNA partner is first processed to yield long single-stranded regions. This single-stranded DNA (ssDNA) is then coated by RecA-type recombinase proteins, forming a nucleoprotein filament (1,2). RecA-type recombinases include, in addition to bacterial RecA, archaeal RadA, and eukaryotic RAD51. These recombinases assembled into nucleoprotein filaments on ssDNA are the catalytic core of homologous recombination responsible for aligning homologous sequence and driving strand exchange between the ssDNA in the filament and homologous double-stranded DNA (dsDNA).

RAD51, RecA, and RadA all form structurally similar helical nucleoprotein filaments, despite their limited amino acid sequences conservation (2). These recombinases do have highly conserved ATPase domains (3,4) and ATP binding is essential for filament formation (2). Structural characterization of these nucleoprotein filaments has almost exclusively been performed using static methods, which resulted in emphasizing regularity. However, even static methods reveal variation in filament structure, often depending on the nucleotide cofactor bound, indicating flexibility and possibly dynamic rearrangements (3–6). The effect of different nucleotide cofactors on filament structure can be explained by the location of their binding site at the interface between adjacent monomers in the DNA-bound filament (2,3,7). Electron-microscopy studies revealed that RAD51 filaments have approximately six monomers per helical turn, and each monomer covers 3 nucleotides (nt) or base pairs (bp) (4,8,9). Similar to RecA, the length of the DNA substrate within the RAD51-DNA filament is maximally extended by 50% compared to the length of B-form DNA (8,10).

---

*To whom correspondence should be addressed. Tel: +31 15 2786094; Fax: +31 15 2781202; Email: c.wyman@erasmusmc.nl, c.dekker@tudelft.nl
Present address:
Ralf Seidel, Biotechnological Center, Dresden University of Technology, Tatzberg 47-51, 01307 Dresden, Germany.

For RecA, the kinetics of filament formation has been extensively characterized (11–15). In particular most recently using time-resolved spFRET (15) and fluorescently labeled RecA (14), a detailed quantitative picture on nucleation and growth of RecA filaments has been obtained. Due to pentameric nucleation but monomeric growth there are conditions, where nucleation is relatively inefficient but filament extension very efficient (here referred to as cooperative filament formation) under which RecA forms very long (>10 kb) continuous filaments. In contrast, RAD51 filament formation is less well characterized. Recent work has shown that RAD51 filaments are irregular in many conditions indicating possible dynamic rearrangements (6,9,16). It has been suggested in those works that the dynamic nature of RAD51-ssDNA filaments may be an important aspect of strand exchange activity (6,16). Analysis of the kinetics of human RAD51 filament formation has been done only with short oligonucleotides (17). We set out to determine from similar kinetic measurements the parameters of dynamic filament formation, specifically nucleation and extension rates, on a quantitative level. For this we use magnetic tweezers, which allow monitoring the real-time dynamic behavior of RAD51-DNA filament formation and disassembly on individual molecules of both ss- and dsDNA of several kilobase in length.

Here, we measured human RAD51 filament formation for a set of controlled reaction conditions that are known to allow or inhibit filament dissociation (6,18) in order to decouple filament growth and dissociation. We compared data sets with extensive Monte Carlo simulations from which we could deduce kinetic parameters of the reaction. Binding of RAD51 to both ss- and dsDNA in the presence of ATP was not strongly cooperative, defined here as the ratio of filament-extension to nucleation rates. At any concentration of RAD51, nucleation played a dominant role in filament formation, in contrast to RecA for which lower concentrations allow infrequent nucleation events followed by rapid filament extension. Removal of RAD51 from the buffer resulted in filament disassembly at multiple positions along the tethered dsDNA molecule, if ATP hydrolysis was allowed. Nucleoprotein filament formation on ssDNA was more complex and dynamic, due to the more prominent role of dissociation on ssDNA. Our results indicate that the RAD51 filaments consist of multiple short filament patches.

MATERIALS AND METHODS

RAD51 purification

The human RAD51 protein was purified as described (6).

DNA substrates

Nicked 8 kb dsDNA with biotinylated and digoxigenin-modified ends was made as described previously (11). A ssDNA construct was prepared as follows. First a double-stranded 8660 bp DNA fragment was produced by PCR, using λ-DNA as a template and primers sequences 5′-AACTCAGCTCACCGTCGAACA and 5′-AAAAG AAATTCCCTCAAATGGACGCCGGATGAC, which was 5′ biotinylated. After purification, the PCR-fragment was digested close to the non-biotinylated end using ApaI at 30°C for 1 h. After this, the ApaI-treated extremity was ligated to a 700 bp PCR fragment containing several digoxigenin-modified dUTP bases and an ApaI ligatable end. The resulting DNA construct was incubated with superparamagnetic 2.8 μm streptavidin-coated beads (Dynal, Oslo) for 30 min at room temperature. Subsequently the bead-bound DNA was denatured by addition of 50 μl 0.1 M NaOH for 30 min at room temperature, in which the biotinylated single DNA strand bound to the magnetic beads was separated from the non-biotinylated complementary strand. Using an external magnet a pellet of the magnetic beads was formed followed by removal of the supernatant. The magnetic beads were re-suspended in 10 mM Tris–HCl (pH 8.0) and 1 mM EDTA, and deposited in the flow cell.

Magnetic tweezers

A magnetic tweezers setup was used in these experiments as described (19). By using image processing, 5 nm position accuracy of the bead was obtained in all three dimensions (20). To exclude the effect of thermal drift, all positions were measured relative to a 3.2 μm polystyrene bead (Bang Laboratories, Carmel, IN) fixed to the bottom of the flow cell.

Flow cell

Polystyrene beads as well as DNA constructs carrying a magnetic bead at one end were anchored to the bottom of a flow cell as described elsewhere (20). The force-extension curve of single DNA molecules was measured (Figure 1B). After conformation of the correct contour and persistence lengths, experiments were started by addition of RAD51. All measurements were carried out at 25°C.

RAD51/DNA reactions

The flow-cell final volume was ~100 μl. All reactions were done in 25 mM Tris–HCl (pH 7.5), 5 mM $MgCl_2$ or $CaCl_2$, 25 mM KCl, and 1 mM DTT. RAD51 and ATP [final concentrations 187 nM RAD51 (unless stated otherwise) and 1 mM ATP] were added into the cell. Interaction of RAD51 with the tethered DNA molecule was monitored through measurement of the height of the magnetic bead.

Monte Carlo simulations

Binding of RAD51 onto a DNA substrate was modeled using Monte Carlo simulations. A similar simulation has previously been done for RecA (21). A 1D array was used to mimic the DNA substrate containing a number of elements equivalent to the number of nucleotides or base pairs of the DNA molecule of interest. In the case of ssDNA the array contained 8660 elements, and for dsDNA 8000. RAD51 filament assembly was described by nucleation followed by growth that extended the nucleation point. Simulations were done with various binding units consisting from 1 to 5 RAD51 monomers. Upon binding of RAD51 to the DNA substrate,

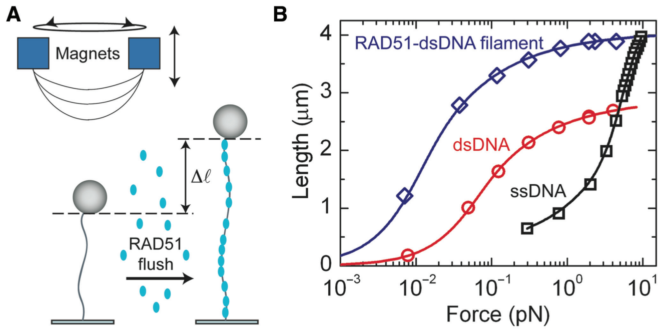

Figure 1. (**A**) Schematic drawing of the magnetic tweezers setup. A DNA molecule is attached at one end to the bottom of the flow cell and at the other end to a magnetic bead. This molecule can be stretched using a pair of magnets placed above the flow cell. The bead position and thus the end-to-end distance of the DNA molecule is determined using video microscopy and image analysis. In such a setup, the interaction of RAD51 with DNA can be followed in real time because binding induces a change in end-to-end distance of the tethered molecule. (**B**) The tethered molecule in the setup is characterized using force-extension measurements to confirm a correct contour and persistence length. The force-extension behavior of dsDNA is fit using the worm-like chain model (red line) yielding a contour length of 2.9 ± 0.1 μm and a persistence length of 49 ± 3 nm, whereas ssDNA displays a different flexibility behavior (black line as a guide to the eye) which cannot be described by worm-like chain (45). After filament formation in the presence of Ca^{2+}, the DNA molecule is elongated and stiffened yielding a contour length of 4.0 ± 0.1 μm and a persistence length of 268 ± 17 nm (blue line) for this particular case.

the protein was assumed to cover 3 nt or base pairs per monomer, and to elongate the binding site length to a value corresponding to 50% compared to the base–base spacing in B-form DNA. Varying the elongation of the binding site between 45 and 55% only changed the obtained increase in end-to-end distance and not the rates for nucleation and filament extension.

Nucleation was allowed to occur at any point along the entire molecule. In the Monte Carlo simulations, the nucleation step was simulated as follows: a value was randomly extracted from a uniform distribution yielding a value between 0 and 1. If this value was smaller than a given threshold corresponding to the set nucleation rate for the entire molecule, a RAD51 oligomer was bound. The binding location was deduced from a second random number between 0 and 1 that was extracted from a uniform distribution that was multiplied by the number of elements in the 1D array. Binding of a n-mer occurred only when this site plus the following $3n - 1$ sites were not covered by another protein, to account for the fact that each protein covered 3 nt or base pairs (cf. Figure 6A).

Subsequently, we evaluated all nucleation sites where filament extension could occur. For each site, a value was extracted from a uniform distribution and compared to a given threshold corresponding to the set rate of filament extension for a single filament patch. If this value was smaller than the threshold, the filament was extended by an oligomeric-binding unit if the next $3n$ nucleotides or base pairs were not already covered by protein. Extension was only permitted into the direction of higher numbers in the 1D array.

The probabilities for nucleation and growth per time step were taken so small, that the chance of two binding events within a single Monte Carlo step was negligible. The threshold values, which are rates expressed in units (Monte Carlo step)$^{-1}$, convert into kinetic rates expressed in s^{-1} by adjusting the time axis of the Monte Carlo growth curve to the experimental growth data. For every Monte Carlo step, the end-to-end distance of the DNA substrate can be calculated by multiplication of all the protein-covered elements in the 1D array by 0.51 nm, and the uncovered ones by 0.34 nm. To account for the entropic coiling of DNA at the specific stretching force applied, the resulting length is decreased according to an amount expected for a worm-like-chain polymer (22). This means that in the force regime probed here, the end-to-end distance is smaller than the crystallographic contour length. Whereas our simple modeling involved filament extension and disassembly in a unidirectional fashion, essentially the same results are found if extension and disassembly occur in both directions, albeit with two slightly different values for the rates that change by a factor up to 2.

In those cases where disassembly was considered, we additionally allowed dissociation to occur after the filament extension step. At each end of a filament patch opposite to the filament-extension end (i.e. towards lower numbers in the array), a value was extracted from a uniform distribution and if this value was smaller than the threshold set by the dissociation rate, the monomer dissociated and a vacancy was created. Alternatively, dissociation was considered at all monomer sites, where the above procedure was extended to all bound RAD51 proteins. In the case of ssDNA, disassembly was modeled in two steps. In the first step, the monomer remained bound, but the contour length of the DNA substrate changed from 0.51 into 0.459 nm [a change of the helical pitch from 92 to 82 Å (5,23)] presumably due to ATP hydrolysis. A value was extracted from a uniform distribution and if this value was smaller than the threshold set by the hydrolysis rate, the monomer underwent this conformational change. This was followed by dissociation presumably through the release of ADP, incorporated as described above.

The Monte Carlo simulated profiles at different ratios between nucleation and filament extension were fit to the experimental data by adjusting the time axis of the Monte Carlo growth using a least-squares method (Figure 7A). For every data set, a best value for the ratio and the time axis was extracted this manner. The average values with the standard deviation mentioned in the main text were calculated from multiple experiments.

RESULTS

Our magnetic tweezers (19,20) single-molecule technique allows monitoring a ‘long’ (~8 kb) individual ss- or dsDNA molecule, which is bound at one end to the surface of a flow cell and at the other end to a magnetic bead, and stretched by a pair of external magnets (Figure 1A). Video microscopy is used to measure,

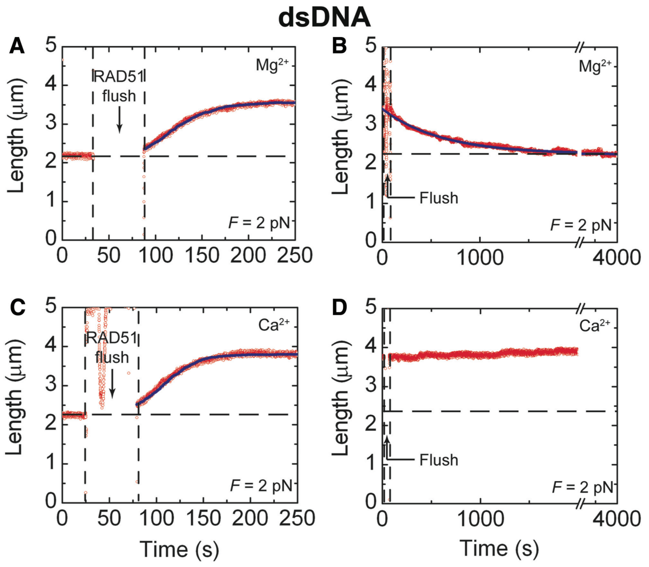

Figure 2. RAD51 filament assembly and disassembly on dsDNA. (A) An 8 kb dsDNA molecule extends by 45% after flushing in 187 nM RAD51 in the presence of 25 mM Tris–HCl (pH 7.5), 5 mM $MgCl_2$, 25 mM KCl, 1 mM DTT and 1 mM ATP. (B) After removal of free RAD51 in solution, disassembly of a RAD51-DNA filament is observed in the presence of Mg^{2+}. (C) In the presence of Ca^{2+} instead of Mg^{2+}, a binding behavior similar to that of Mg^{2+} is observed. (D) In the presence of Ca^{2+}, however, disassembly is not observed and the end-to-end distance remained unaffected upon the removal of free RAD51 in solution. The solid lines in the figures show the result of Monte Carlo simulations using a rate for nucleation and filament extension to describe filament assembly. For the disassembly reaction, a single disassembly rate is taken into account. Solid lines in panels A and B are fits, whereas the line in panel C is plotted without any adjustable parameters. Dashed horizontal lines indicate the DNA end-to-end length in the absence of RAD51. Reaction rates were determined from the average of multiple experiments for each condition ($n \sim 10$).

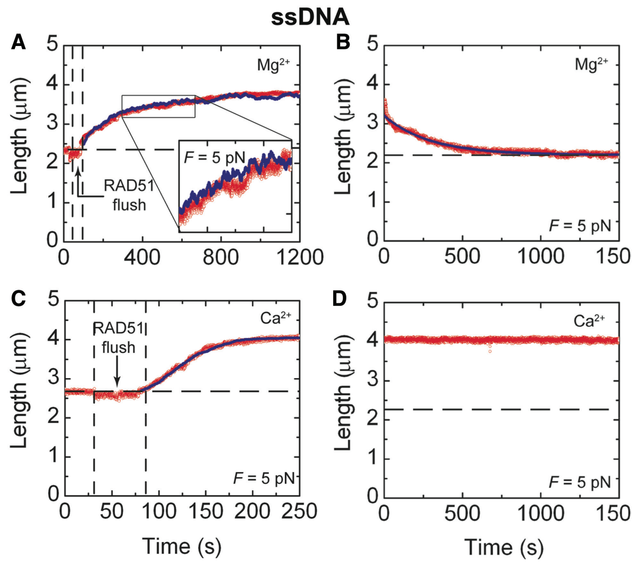

Figure 3. RAD51 filament assembly and disassembly on ssDNA (A) In the presence of Mg^{2+} and 1 mM ATP, 187 nM RAD51 starts extending an 8.6 knt ssDNA molecule directly after the flush is stopped. In contrast to dsDNA (Figure 2C), the observed extension was slow and very irregular, as emphasized in the inset. The blue line is a fit based on the Monte Carlo simulations allowing disassembly per filament end. Nucleation and growth rates where taken from the Ca^{2+} data (see subsequently). (B) After removal of free RAD51 in solution, the DNA end-to-end distance decreased, indicating disassembly of the RAD51-ssDNA filament. The solid line is a fit with a double exponential (see text). (C) In the presence of Ca^{2+}, the observed growth profile is similar to the one observed on dsDNA. The solid lines are fits based on the Monte Carlo simulations allowing only nucleation and growth. (D) After removal of free RAD51 in solution, the end-to-end distance remained constant when Ca^{2+} is present. Dashed horizontal lines indicate the DNA end-to-end length in the absence of RAD51. Reaction rates were determined from the average of multiple experiments for each condition ($n \sim 10$).

with high temporal (60 Hz) and spatial resolution (5 nm for the position of the magnetic bead), the DNA end-to-end distance in real time. Upon adding RAD51 to the flow cell, the DNA end-to-end distance increased, consistent with the formation of a DNA-RAD51 nucleoprotein filament that extends the DNA. Typical examples of time traces for the assembly of RAD51 onto and disassembly from DNA are shown in Figures 2 and 3. The observed behavior on dsDNA was independent of force in the range of 0.1–4 pN (Figures S1 and S2). Reaction rates were determined from the average of multiple ($n = 5$–10) experiments for each condition.

Assembly/disassembly of RAD51 onto/from dsDNA

We first discuss our results for the interaction of RAD51 with torsionally unconstrained, i.e. nicked, dsDNA. Filament assembly was monitored by introducing RAD51 and ATP into the flow cell which caused an increasing DNA end-to-end distance immediately after the buffer flow was stopped (Figure 2A). Subsequently, the extension rate of the DNA end-to-end distance accelerated, slowed down again, and reached a final constant value. This typical sigmoidal extension profile indicates filament formation. Already at a qualitative level, we can conclude that the cooperativity of growth must be substantially lower than that of RecA on dsDNA where nucleation is much slower than filament extension and completely linear growth profiles are observed after a fairly long ($\sim 10^2$ s) lag time (11).

The increase in DNA tether length observed in the presence of RAD51 reflects a net association behavior, likely consisting of both association and dissociation contributions. In order to disentangle these contributions, we first analyzed dissociation alone. After the filament assembly saturated, dissociation of RAD51 from dsDNA was initiated by exchanging the buffer in the flow cell for one without RAD51 but with ATP and Mg^{2+}. This allows continuous ATP hydrolysis by the RAD51 filament. The presence of ADP or the absence of any nucleotide cofactor in the flow cell during disassembly did not change disassembly behavior relative to the conditions with ATP (data not shown). The disassembly curve, monitored as a decrease in DNA end-to-end distance (Figure 2B) had an exponential decay with a time constant of 589 ± 27 s ($n = 7$). After 1 h, the decrease in end-to-end distance reached a plateau corresponding to the length of bare dsDNA at the stretching force applied.

Recombinases such as RAD51 are DNA-dependent ATPases, where the type of bound nucleotide cofactors determine the dynamic interactions between recombinases and DNA (6,24). Filament assembly was therefore also measured in the presence of ATP and Ca^{2+}, conditions that allow ATP binding by RAD51 but greatly reduce ATPase activity (18). The growth profiles (Figure 2C) were quite similar to those observed in ATP and Mg^{2+} buffer. The concentration of RAD51 in the flow cell was varied between 19 and 384 nM. At concentrations below 45 nM no increase in end-to-end distance was observed within 2 h. At higher concentrations, growth curves similar to those shown in Figure 2C (obtained at 187 nM) were observed. However, the rate of filament formation increased with concentration. The end-to-end distance of the molecule did 'not' decrease, upon removing free RAD51 for a buffer containing ATP and Ca^{2+} (Figure 2D). This shows that filament disassembly is indeed inhibited, yielding stable filaments when ATP hydrolysis by RAD51 is greatly reduced, i.e. RAD51 is maintained in an ATP-bound form (18).

Assembly/disassembly of RAD51 onto/from ssDNA

We also studied the dynamics of RAD51 filament assembly on ssDNA, which is the substrate relevant for initiating homology search, strand invasion and joint molecule formation. A kinetic description of the interaction between RAD51 with ssDNA that result in filament formation is important for understanding homologous recombination. After adding RAD51 and ATP to the flow cell, the end-to-end distance of ssDNA started to increase immediately (Figure 3A). Compared to dsDNA, extension was much slower (note the different time scales in Figures 2A and 3A) and much more irregular. We observe strong fluctuations in the actual growth velocity, plus occasional shrinkage (see Figure 3A and its inset). After ~300 s, the extension was followed by much slower and interrupted extension until it reached a final plateau after 800 s where no further elongation or shortening was observed.

Dissociation of RAD51 from ssDNA was initiated as before, by exchange of the buffer in the flow cell for one without RAD51 but with ATP and Mg^{2+}. This allows continuous ATP hydrolysis by RAD51. The end-to-end distance of the RAD51-ssDNA molecule decreased after removing free RAD51 (see Figure 3B). The behavior observed here revealed two dissociation processes, a fast and a slow one, and was accordingly fit with a bi-exponential decay with time constants of 26 ± 6 s and 362 ± 45 s ($n = 9$). After about 30 min, the decrease in end-to-end distance reached a plateau corresponding to the length of bare ssDNA. The presence of ADP or the absence of any nucleotide cofactor in the flow cell during disassembly did not change the values of the exponential time constants relative to the conditions with ATP (data not shown). In conditions that allow ATP binding by RAD51 but greatly reduce ATPase activity, e.g. with ATP and Ca^{2+} instead of Mg^{2+} (18), the end-to-end distance of the molecule did not decrease after removing free RAD51 (see Figure 3D). RAD51-ssDNA filaments formed in the presence of Ca^{2+} did not dissociate and were stable, in contrast to those in the presence of Mg^{2+}. These single-molecule experiments show that inhibition of ATP hydrolysis results in stable RAD51 filaments on ssDNA.

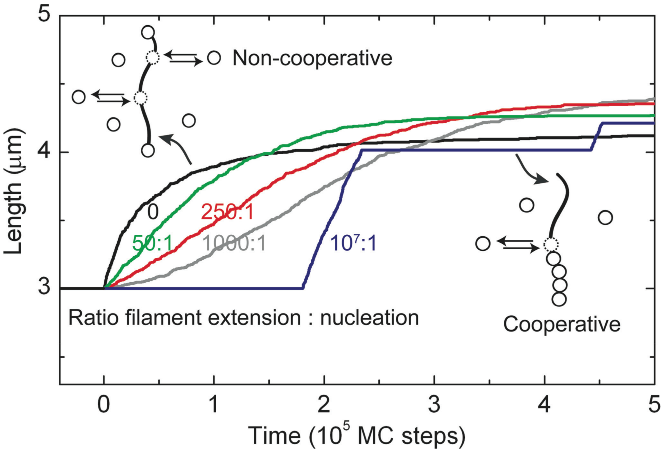

Figure 4. Results from Monte Carlo simulations for the binding of a recombinase on DNA for different levels of cooperativity. If only random binding (nucleation) occurs along the contour length of the DNA molecule (non-cooperative binding, see top left), an exponential growth profile is obtained (black line). The obtained elongation is smaller than 50% due to the presence of nucleotide positions on the DNA where no further binding can occur. However, if filament extension is fast compared to nucleation, e.g. for a ratio larger than 10^6 (strong cooperative binding, see bottom right), the growth profile becomes linear and the molecule can be fully covered by the protein up to the maximum 50% elongation (blue line). For intermediate ratios between filament extension and nucleation, sigmoid-like shaped growth profiles are observed (green, red, gray lines).

Interestingly, the growth profile of RAD51 on ssDNA in the presence of Ca^{2+} was substantially different from that in the presence of Mg^{2+} (Figure 3C). In ATP and Ca^{2+} conditions, the end-to-end distance of the molecule increased immediately after flushing, and the growth profile had a smoother and sigmoidal shape reaching a final plateau after about 100 s. The assembly behavior of RAD51 in the presence of ATP and Ca^{2+} is very similar for ss- and dsDNA (cf. Figures 2C and 3C). In both cases, RAD51 dissociation is substantially slower than filament formation, whereas RAD51 dissociation plays a more prominent role in the assembly process on ssDNA.

Monte Carlo simulations of nucleoprotein filament formation

In order to understand the mechanistic processes that lead to the observed growth profiles, we modeled the process of nucleoprotein filament formation. Our single-molecule experiments allow modeling of the (dis)assembly processes in great quantitative detail. The simplest model of nucleoprotein filament formation involves two processes: initial nucleation followed by unidirectional filament growth (12,13). For the case of nucleation only, i.e. when the protein displays no enhanced binding at a filament end (non-cooperative growth), an exponential growth profile is expected (cf. black line in Figure 4). The other extreme is highly cooperative filament formation. In this case, a single nucleation event is followed by fast filament extension, i.e. after a lag time (set by the nucleation rate) one obtains a linear growth profile (cf. blue line in Figure 4), as has been observed for RecA (11,12). In between the two extremes, the slope of the growth curve obtained depends on the ratio between nucleation and filament growth.

We modeled the kinetics of RAD51 filament formation on DNA using Monte Carlo simulations. RAD51 monomers are taken to bind 3 nt or base pairs of DNA and to extend DNA by 50% compared to B-form DNA. For these parameters we use the best-defined values determined from the length of DNA circles that were fully coated by Rad51 (8), the protein-filament pitch and DNA-binding studies (25). We choose to model the binding of RAD51 to DNA in binding units of either monomers or multimers (e.g. 5 monomers). Binding of individual RAD51 monomers or multimers through nucleation and filament extension on a theoretical DNA molecule was performed during multiple ($\sim 10^5$) time steps (for details see Materials and Methods section). 'Nucleation' denotes binding of a monomer or a multimer at an unoccupied DNA position, not adjacent to already bound proteins, whereas we define 'filament growth' as binding to a site directly adjacent to one that is already occupied. Because RAD51 does not show affinity for a particular sequence, nucleation occurs randomly along the entire molecule.

Using these simulations, we obtained growth profiles at different ratios between filament growth and nucleation (Figure 4). After a first nucleation event, the extension of the DNA molecule increases due to the extension of the filament. Depending on the ratio between rates for filament extension and nucleation, henceforth called the cooperativity number, new nucleation loci are created followed by extension into filament patches. The process ends when the molecule has no more free binding sites large enough to accommodate binding of another monomer or multimer, depending on the situation being modeled. The simulations yield information on the kinetics of growth and also on the resulting final elongation of the RAD51 filament. In the case of nucleation only, and excluding RAD51 diffusion along DNA, the final elongation is smaller than the upper bound of 50%, because gaps remain of free DNA with a size smaller than the binding site. This is due to the random nature of binding. If filament extension (which is gap-free by definition) dominates over nucleation, fewer gaps are formed, and a longer final filament length is obtained. The final extension of the molecule is thus dependent on the ratio between the rates of filament extension and nucleation (Figure 6C).

Growth by monomers or multimers

Using the extension profiles generated with the Monte Carlo simulations (Figure 4), rates for nucleation and filament extension on both ss- and dsDNA were determined from the experimental data. In the presence of ATP and Ca^{2+}, disassembly is practically inhibited, as shown above. We therefore can neglect disassembly and fit the growth profiles obtained in the presence of Ca^{2+} with a growth-only model (see Materials and Methods section and Figure 7A for an example) generated with different rates and binding sizes for nucleation and filament extension (Figure S3). This yields accurate numbers for the nucleation and filament extension rates. Below we address these (see next section), but first we comment on the size of the RAD51-binding unit to DNA.

We can determine the minimum size of the binding unit from an analysis of the dependence of the rates on concentration of RAD51. This can be separately analyzed for filament nucleation and extension. The mathematical description of a monomer binding to DNA follows a Michaelis–Menten relation,

$$k_i = \frac{k_{i,\max}[\mathrm{RAD51}]}{S_{0.5} + [\mathrm{RAD51}]}, \qquad \mathbf{1}$$

where k_i is the observed binding rate, $k_{i,\max}$ the maximum binding rate, [RAD51] the concentration of RAD51 and $S_{0.5}$ the substrate concentration where half-maximal activity occurs. If, however, binding occurs through a preformed multimer or a set of monomers binding in a sequential coordinated fashion, then binding is described by the Hill relation,

$$k_i = \frac{k_{i,\max}[\mathrm{RAD51}]^n}{S_{0.5}^n + [\mathrm{RAD51}]^n}, \qquad \mathbf{2}$$

where n is termed the Hill coefficient, which is a measure for the minimum size of the binding unit (26). A Hill coefficient of $n = 1$ indicates single monomer binding, whereas a Hill coefficient $n > 1$ indicates the binding of n monomers in a coordinated fashion or binding through a preformed multimer.

Fitting the data of the nucleation rate versus RAD51 concentration by the Hill equation, yielded a Hill coefficient of 4.3 ± 0.6 (Figure 5A). We note that the result is independent of the chosen binding size in the Monte Carlo simulations for nucleation (see Figure S3 and Table S1). This number gives a lower bound of the RAD51 nucleation unit. This is in good agreement with a Hill coefficient previously determined for interaction of RAD51 with ssDNA oligonucleotides (17). Describing the concentration-dependent nucleation rate with the Michaelis–Menten relation [Equation (1) dotted line in Figure 5A] clearly does not fit the data. Based on these data we employed a multimeric and not a monomeric nucleation unit in our modeling.

Separately fitting the data for the extension rate of individual filament patches versus RAD51 concentration by the Hill equation, yielded a Hill coefficient of 4.4 ± 0.5 (Figure 5B), again independent of the chosen binding size in the Monte Carlo simulations for extension per filament patch (Figure S3 and Table S1). This number gives the size of the apparent RAD51 unit participating in the filament extension. Describing the concentration-dependent extension rate per filament patch with the Michaelis–Menten relation again does not fit the data. Based on these data we also employed a multimeric and not a monomeric binding unit for extension per filament patch.

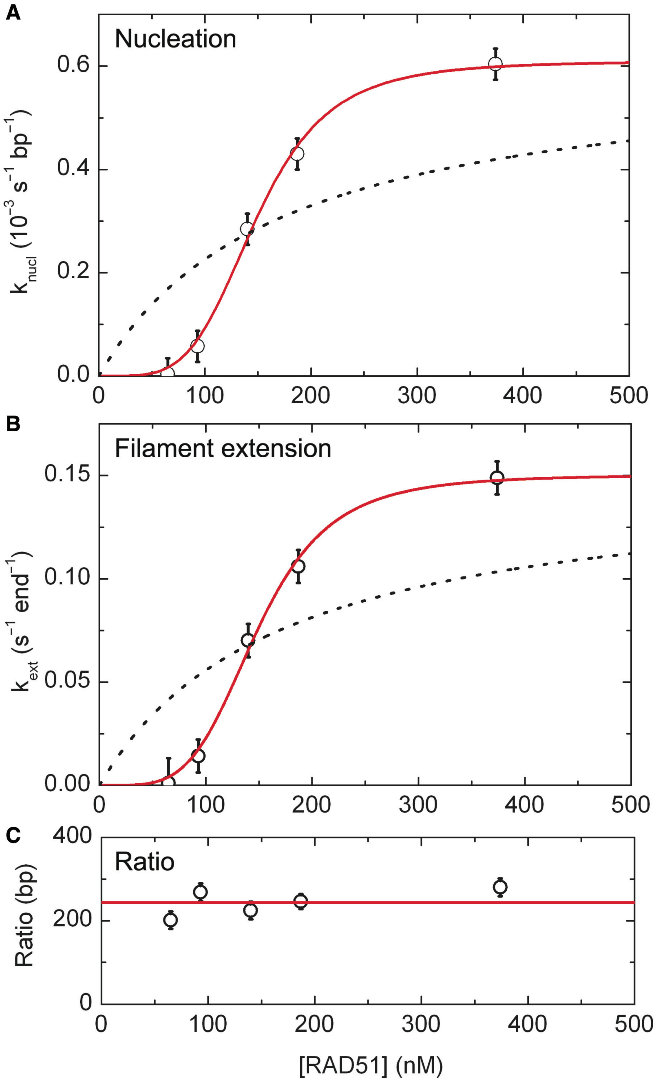

Figure 5. Concentration-dependent RAD51 filament assembly rates on dsDNA in the presence of Ca^{2+} and 1 mM ATP. **(A)** Nucleation rate. The nucleation data was fit with the Hill equation, yielding a Hill coefficient $n = 4.34 \pm 0.56$, a substrate concentration where half-maximal activity occurs $S_{0.5} = 149 \pm 4$ nM, and a maximum nucleation rate $k_{i,\max} = (0.61 \pm 0.03) \times 10^{-3}\,\mathrm{s}^{-1}\,\mathrm{bp}^{-1}$. **(B)** Extension rate per filament patch. The extension rate per filament patch was fit with a Hill coefficient $n = 4.35 \pm 0.46$, $S_{0.5} = 149 \pm 4$ nM, and $k_{i,\max} = 0.150 \pm 0.006$ pentamers s^{-1} end^{-1}. **(C)** The ratio between extension per filament patch and nucleation is found to remain constant as a function of [RAD51]. The dotted lines correspond to binding rates that follow a Michaelis–Menten relation, indicative of monomeric nucleation and extension per filament patch. This clearly fails to fit the data.

Though the rates of both extension per filament patch and nucleation were strongly concentration dependent, the ratio between extension per filament patch and nucleation was found to be concentration independent (Figure 5C). For different concentrations of RAD51, the shape of the growth profiles was thus preserved.

Quantifying nucleation and filament extension rates

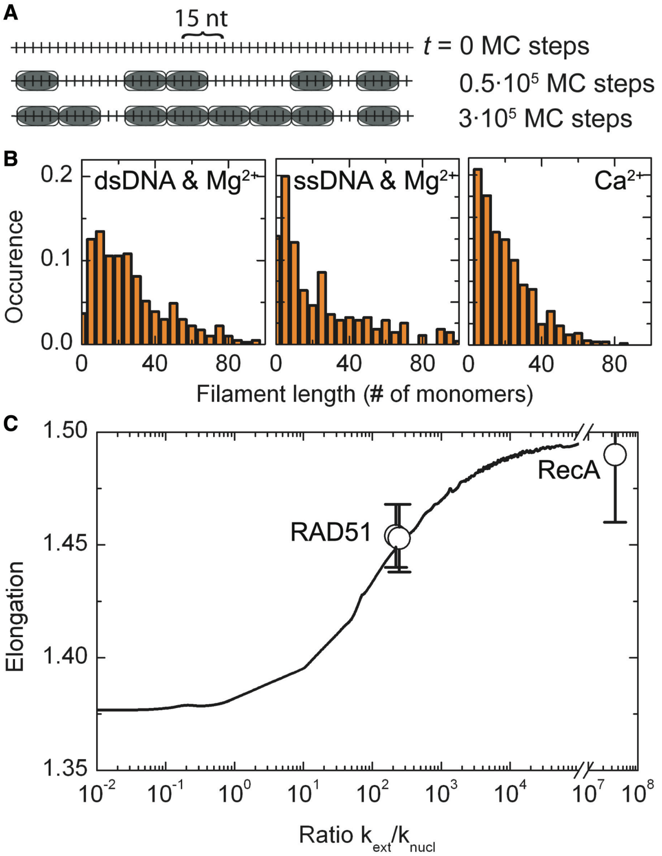

Figure 6. **(A)** Snapshots of RAD51-DNA filament patches at different times during a Monte Carlo simulation in the absence of dissociation. This simulation is carried out for $k_{\mathrm{nucl}} = 5 \times 10^{-7}$ site^{-1} (Monte Carlo step)$^{-1}$, $k_{\mathrm{ext}} = 1 \times 10^{-4}$ (Monte Carlo step)$^{-1}$. Due to the fast nucleation rate, multiple filaments are formed along the DNA substrate. As a RAD51 pentamer covers 15 nt or base pair upon binding, nucleation or filament extension can only occur if sufficient space is available. In the bottom panel, the simulation has reached its final state since no further pentamers can bind. **(B)** Filament-length distribution in the final state for dsDNA in the presence of Mg^{2+}, ssDNA with Mg^{2+} and DNA with Ca^{2+}. The distributions for ss- and dsDNA with Ca^{2+} are practically identical. **(C)** Final elongation of a RAD51-DNA filament as a function of the ratio between rates for filament extension and nucleation. For low $k_{\mathrm{ext}}/k_{\mathrm{nucl}}$, a plateau of 38% extension is obtained, whereas for high $k_{\mathrm{ext}}/k_{\mathrm{nucl}}$ the full 50% extension can be reached. The open circles represent the elongations of ss- and dsDNA by RAD51 obtained in the presence of Ca^{2+} in our measurements, and the elongation by RecA on dsDNA taken from Ref. (11).

In the presence of Ca^{2+}, the rates of nucleation and extension per filament patch of RAD51 on DNA were determined from growth profiles. In the case of dsDNA and 187 nM RAD51, the least-squares-fit residue was minimal at a ratio of extension per filament patch versus nucleation of (246 ± 18):1 bp ($n = 5$), yielding an excellent fit for the growth profile as shown by the blue line in Figure 2C. The growth rate per filament end was 0.106 ± 0.008 pentamers s^{-1}, and the nucleation rate was $(4.3 \pm 0.3) \times 10^{-4}\,\mathrm{s}^{-1}\,\mathrm{bp}^{-1}$. For ssDNA, the best fit was obtained at a ratio of extension per filament patch versus nucleation of (220 ± 16):1 nt ($n = 5$) (see Figure 7A and its inset), indicated by the blue line in Figure 3C. The simulations yielded a growth rate per filament of 0.085 ± 0.006 pentamers s^{-1} and a nucleation rate

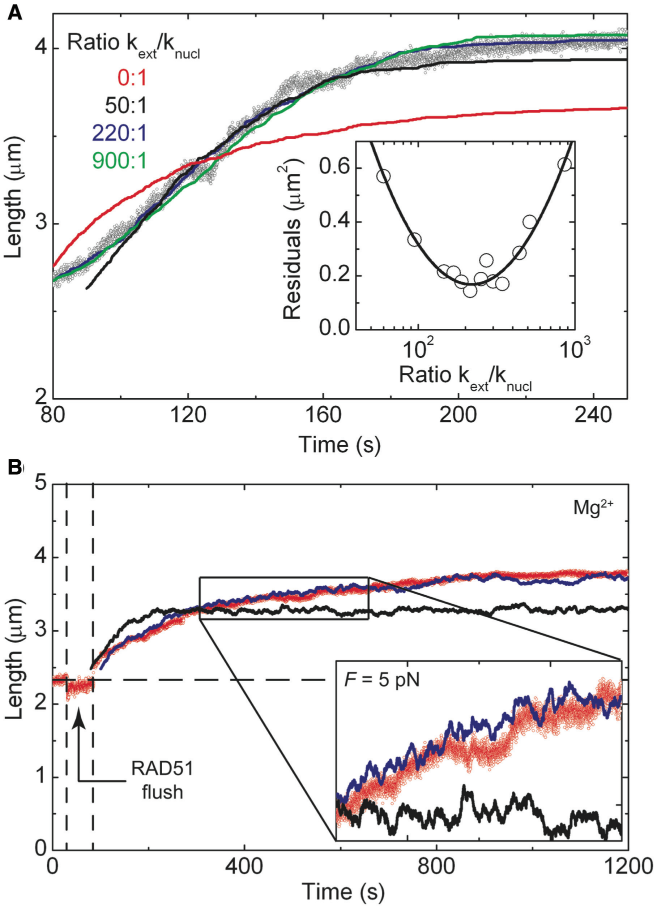

Figure 7. (**A**) Growth curves from Monte Carlo simulations (solid lines) at different ratios between filament extension and nucleation fitted to an experimental binding profile of RAD51 on ssDNA in the presence of Ca^{2+} (gray circles). Inset shows the least-squares-fit residuals obtained for several ratios of k_{ext}/k_{nucl}. As can be seen in the inset, the best fit is obtained at a ratio of 220:1, where the least-squares-fit residuals are minimal. The minimum is determined using a parabola. (**B**) Monte Carlo simulations of RAD51 filament formation on ssDNA allowing disassembly during growth per monomer (black) or per filament end (blue), without changing the rates for nucleation and growth.

of $(3.9 \pm 0.3) \times 10^{-4}\,s^{-1}\,nt^{-1}$ for ssDNA. Varying the functional binding unit in the Monte Carlo simulations between 4 and 6 RAD51 monomers based on the Hill coefficient yielded similar profiles (data not shown), with rates that differed less than 3% from the values for RAD51 pentamers. Using these simulated extension profiles, rates for nucleation and extension per filament patch on both ss- and dsDNA can be accurately determined from the experimental data (summarized in Table 1).

Quantifying dissociation

In the absence of Ca^{2+} and presence of Mg^{2+}, dissociation of RAD51 needs to be considered as well. This occurs upon filament disassembly but also during filament assembly. We extracted the dissociation rate of RAD51 from DNA from the disassembly profiles in the presence of Mg^{2+} by fitting them with time traces generated in the Monte Carlo simulations. Disassembly is assumed to occur either for all monomers equally, or for monomers only at the end of the filament patches (as for RecA) (13), whose distribution was obtained in the simulations (Figure 6B). In the simulations we separately considered both cases (see Material and Methods section), each providing exponentially decaying disassembly profiles. For dsDNA, a dissociation rate per filament patch end of $0.021 \pm 0.001\,s^{-1}$ was obtained (27), or alternatively, a dissociation rate per monomer of $(1.70 \pm 0.08) \times 10^{-3}\,s^{-1}$ if dissociation is allowed for all monomers regardless of their position. The result of the fit is denoted by the blue line in Figure 2B.

Table 1. Rates and structural parameters for RAD51 filament formation on ss- and dsDNA at 187 nM RAD51

	RAD51	
	dsDNA	ssDNA
Nucleation ($nt^{-1}\,s^{-1}$)	$0.00043^{p} \pm 0.00003$	$0.00039^{p} \pm 0.00003$
Growth (s^{-1})	$0.106^{p} \pm 0.008$	$0.085^{p} \pm 0.006$
Filament end dissociation (s^{-1})	$0.021^{m} \pm 0.001$	$0.35^{m} \pm 0.08$ $0.036^{m} \pm 0.004$
Ca^{2+}		
Elongation (%)	45.3 ± 1.5	45.4 ± 1.4
Coverage (%)	91 ± 3	91 ± 3
Mg^{2+}		
Elongation (%)	44.1 ± 0.8	22.6 ± 0.7
Coverage (%)	88.2 ± 1.6	68.1 ± 0.6

Standard errors obtained from measurements of about 10 individual time traces are indicated. The symbols *p* and *m* denote the interaction size of the protein with the DNA substrate as respectively a pentamer and monomer.

In the case of ssDNA, the disassembly curve displayed a double exponential. For the disassembly behavior on ssDNA in the Monte Carlo simulations, we therefore used two dissociation rates to model this bi-exponential behavior: (i) a rate representing a conformational change of the bound RAD51 monomer presumably due to ATP hydrolysis, followed by (ii) a rate representing RAD51 dissociation presumably upon the release of ADP. Due to the relatively rapid ATP hydrolysis and slow dissociation of ADP (28), the RAD51-ATP-ssDNA filament becomes quickly converted to a RAD51-ADP-ssDNA form, which is unable to perform strand exchange (18). It has been shown for RecA that the helical pitch is reduced in the presence of ADP i.e. from 92 Å for the ATP-bound state to 82 Å with ADP (5,23). Therefore we expect that the measured end-to-end distance in the magnetic tweezers shortens if ATP is converted into ADP during ATP hydrolysis, followed by another decrease in end-to-end distance when RAD51 dissociates presumably due to the release of ADP. Modeling of these events for the two different cases considered during dissociation (see Materials and Methods section) shows a bi-exponential disassembly behavior in both cases (blue line in Figure 3B). Dissociation per filament patch end yields rates for ATP hydrolysis of $0.35 \pm 0.08\,s^{-1}$ and RAD51 dissociation of

$0.036 \pm 0.004\,\mathrm{s}^{-1}$, or alternatively regardless of the position of a monomer within the filament an ATP hydrolysis rate of $0.038 \pm 0.009\,\mathrm{s}^{-1}$ and a RAD51 dissociation rate of $(2.8 \pm 0.4) \times 10^{-3}\,\mathrm{s}^{-1}$. These results are summarized in Table 1. All the above rates reduce by a factor 5 if one adopts a pentameric disassembly unit, but the shape of the observed disassembly curve remains exactly the same.

Finally, the growth profiles in the presence of ATP and Mg^{2+} were modeled using the nucleation and extension rates per filament patch obtained in the presence of Ca^{2+}, plus the dissociation rate that was experimentally obtained from the disassembly curves with Mg^{2+}. Extension curves generated in the Monte Carlo simulations with these three obtained rates (i.e. no free fitting parameters) for dsDNA, yielded results in excellent agreement with the observed behavior, see the blue line in Figure 2A.

Similarly, the time traces for RAD51 growth on ssDNA with Mg^{2+} were fit without adjustment of the rates for nucleation, extension per filament patch, ATP hydrolysis and RAD51 dissociation. The result, the blue line in Figure 3A, is again in remarkable agreement with the experimental data. Interestingly, the simulated time trace showed a similar intermittent behavior of growth and occasional disassembly (see Figure 3A and inset of Figure 7B). In Figure 7B, simulated time traces were superimposed on the extension profile for the two models with either dissociation only at ends of filament patches (blue line), or for all bound monomers regardless of their position within the filament patch (black line). The latter clearly does not overlay the observed behavior, whereas the former does. This indicates that RAD51 disassembly does not occur at all monomer sites but instead occurs only at the end of the filament patch.

Final coverage of RAD51-coated DNA

The end-to-end distance observed after filament formation on DNA indicates the extent of coverage by RAD51. As DNA is an entropic coil in solution, the measured end-to-end distance is dependent on the stretching force applied. In order to determine the contour lengths of the RAD51-DNA filament, we carried out force-extension measurements (for typical examples, see Figure 1B). The resulting curves were fitted with the worm-like-chain model where only the contour length and the persistence length are free parameters (29).

In the case of dsDNA, a contour length of $2.75 \pm 0.05\,\mu\mathrm{m}$ ($n = 5$) was obtained before filament assembly, corresponding nicely to the expected length of an 8 kb dsDNA ($8 \times 10^3 \times 0.34\,\mathrm{nm} = 2.72\,\mu\mathrm{m}$). After nucleoprotein filament assembly in the presence of Ca^{2+}, the contour length was $3.99 \pm 0.08\,\mu\mathrm{m}$ ($n = 5$) yielding an elongation of $45.3 \pm 1.5\%$ ($n = 5$). On ssDNA, a contour length of $4.25 \pm 0.04\,\mu\mathrm{m}$ ($n = 5$) was obtained after filament formation, corresponding to an elongation of $45.4 \pm 1.4\%$ ($n = 5$) compared to native B-form DNA consisting of 8.6 knt with a contour length of 2.92 µm. Interestingly, at the assembly/nucleation ratio of 246:1 and 220:1 for respectively ds- and ssDNA, our model predicts due to the incomplete DNA coverage an elongation of $45.04 \pm 0.08\%$ and $44.77 \pm 0.08\%$ ($n = 10$) assuming a 50% extension caused by RAD51 binding, which is in excellent quantitative agreement with both results (Figure 6C). The elastic properties of RAD51-bound DNA also clearly indicate incomplete coverage.

For both substrates, ss- and dsDNA, the stiffness of the RAD51-DNA filament in the presence of Ca^{2+}, given by the persistence length, was $196 \pm 14\,\mathrm{nm}$ ($n = 10$), i.e. increased by a factor 4 compared to bare dsDNA with a persistence length of $49 \pm 2\,\mathrm{nm}$ ($n = 5$) (Figure 1B). A much higher value, of ~1 µm, has been reported for the persistence length of RecA filaments that continuously coat DNA (30). We note, however, due to the almost complete coverage, the gaps of naked DNA between neighboring RAD51 patches will likely not act as free hinges but may experience some steric hindrance. The persistence length of a RAD51-DNA filament we report here provides a lower bound for the stiffness of a RAD51-DNA filament, because the contribution of soft hinges will lower the overall stiffness.

The elongation of the RAD51 filaments in the presence of Mg^{2+} was also determined from force-extension curves before and after filament formation. Elongation of $44.1 \pm 0.8\%$ ($n = 9$) was observed for dsDNA in the presence of Mg^{2+}. The Monte Carlo simulations including dissociation yielded an elongation of $46.1 \pm 0.2\%$ ($n = 10$). Imaging studies on elongation of dsDNA in the presence of ATP and Mg^{2+} reported values of about 40% for RAD51 (6,9), and about 38% for *Saccharomyces cerevisiae* Rad51 (8,10), also indicative of partial coverage.

In contrast, the force-extension curves recorded for RAD51-ssDNA filaments formed in the presence of Mg^{2+} (data not shown) could not be fit well by the worm-like chain model. In the presence of Mg^{2+}, the final RAD51 coverage of ssDNA was only $68.1 \pm 0.6\%$ according to the Monte Carlo simulations, due to ongoing dissociation during assembly. The presence of (long) tracks of bare ssDNA between RAD51 filament patches thus will have a pronounced effect. Microscopy studies of RAD51 filaments on ssDNA also indicate only partial coverage (6,9,16). Because the contour length could not be determined from force-extension curves, we measured the end-to-end distance at 5 pN, because at this force the length of a given ssDNA molecule is equal to the length of an equivalent nucleotide stretch of B-form dsDNA. For our ssDNA construct consisting of 8660 nt and covered for $68.1 \pm 0.6\%$ by RAD51, the end-to-end distance obtained from the Monte Carlo simulations was $3.68 \pm 0.01\,\mu\mathrm{m}$, which is in good agreement with the observed end-to-end distance of the RAD51-ssDNA construct of 3.61 ± 0.11 ($n = 12$) at 5 pN.

Implications for the filament structure

The simulations, which show excellent agreement with our experimental data, allowed us to make conclusions about the structure of the filament that is formed. A single nucleation event followed by subsequent extension leads to the formation of a long continuous filament. For RAD51 however, the finite large rate of nucleation yields many nucleation sites. Extension per filament patch occurs at each site until it reaches the neighboring filament patch.

The random positioning of nucleation sites leads to gaps of bare DNA (up to 14 bases for a pentameric-binding unit) between the filaments. The measured end-to-end distances of the RAD51–DNA complexes clearly indicate partial coverage, as the elongation is less than 50%. This is caused by the formation of multiple filament patches along the DNA molecule, which leave gaps of bare DNA in between (27). These results are consistent with RAD51 behavior observed by Van Mameren *et al.* (31) and argue against RAD51 diffusion along DNA participating in filament formation (32). Diffusion would eliminate gaps between adjacent filaments resulting in full coverage and thus an elongation of 50%, independent of the ratio between nucleation and extension per filament patch. This is not observed in our experiments.

In contrast to expectations, the average length of continuous RAD51 filament patches on dsDNA was found to be very short. In the presence of Ca^{2+}, where ATP hydrolysis is suppressed, the filament patch length distribution obtained from the Monte Carlo simulations for ss- and dsDNA yielded an average filament length of 21 ± 15 (mean ± SD, $n = 578$) RAD51 monomers, see Figure 6B. In the presence of Mg^{2+}, however, the distributions change due to the influence of dissociation. In the case of dsDNA, the average filament length is 30 ± 24 (mean ± SD, $n = 408$) RAD51 monomers. This is consistent with filament patches obtained with sub-saturating amounts of RAD51 (33). On ssDNA, the Monte Carlo simulations yielded an average filament length of 35 ± 43 (mean ± SD, $n = 281$) RAD51 monomers.

DISCUSSION

We have quantitatively described the association and dissociation of RAD51 with ss- and dsDNA using single-molecule measurements and Monte Carlo simulations. The obtained rates are summarized in Table 1. Though direct comparison with RecA is difficult due to variation in reaction conditions and assays, RAD51 has apparently a higher nucleation rate and lower extension rate per filament patch. This is based on the behavior of RecA binding to dsDNA as measured in recent single-molecule experiments done under similar conditions of protein concentration and nucleotide cofactor (14). From those data, we can extract an extension rate at 170 nM RecA of 2–7 monomers s^{-1}, ~10-fold higher than the extension rate we measure for RAD51 (Table 1). The highest nucleation rate at 200 nM would correspond to $6 \times 10^{-7} s^{-1} bp^{-1}$ for a RecA pentamer, or 10^3-fold lower than we measure for RAD51. Comparing the ratio of extension per filament patch to nucleation makes RAD51 filament formation much less cooperative than RecA filament formation, under these conditions.

The behavior of RAD51 that we observe is well described with a multimeric-binding unit for both nucleation and extension per filament patch. We measured DNA length profiles that imply extension in steps equivalent to binding of multimers of on average n RAD51 coordinated monomers where $n = 4.3 \pm 0.5$. A variety of multimeric forms in this range have been described for RAD51 (23,34–36). Furthermore, recent studies reported that RecA nucleates on both ss- and dsDNA as a pentamer (14,15). RecA filament extension was, however, suggested to occur by monomeric association extracted from a novel analytical tool based upon hidden Markov modeling (15). In contrast to this result, our finding for RAD51 indicates the DNA length changes during extension per filament patch involves multimers.

RAD51 forms complexes with both ss- and dsDNA during the course of homologous recombination. RAD51 functions in eukaryotic cells in coordination with many other proteins including the so-called recombination mediators, favoring RAD51 assembly onto ssDNA in need of homologous recombination and disfavoring assembly elsewhere (37). The behavior of RAD51 with DNA that we describe here, provides a baseline for assessing the detailed effect other recombination proteins have on filament assembly and stability. The flexible RAD51 interface domain, a proposed site of molecular hand-off events (36), may be important in determining multimer addition, limiting filament growth rate or effecting filament stability. It will also be important to determine if the described effects of the BRCA2 domains are due specifically to changes in RAD51 filament nucleation, growth, or disassembly rates (38–41).

The intrinsic dynamics of RAD51 filament assembly and disassembly are likely important aspects of homology search and strand-exchange. We observe intermittent assembly dynamics and partial coverage, for RAD51 especially on ssDNA. When ATP hydrolysis is active, interactions between RAD51 and ssDNA are much more dynamic than with dsDNA. With respect to this different behavior of RAD51 on ss- and dsDNA, it is interesting to note that, in contrast to the situation in bacteria, proteins capable of disassociating RAD51 filaments from dsDNA play an important role in mammalian homologous recombination (42). Most notably, the disassembly rate of RAD51 monomers from ssDNA and dsDNA is very different.

Our experiments reveal that during the continuous interplay of assembly and dissociation, short RAD51 filament patches are formed on DNA. These RAD51-DNA patches are separated by tracks of bare DNA that are too short to allow additional RAD51 association (27). Force-extension measurements showed that RAD51-DNA was more flexible than RecA-coated DNA by a factor of 4. The greater flexibility of RAD51-DNA complexes supports the presence of bare DNA gaps. The presence of short interrupted RAD51 filaments explains some aspects of RAD51 strand-exchange reactions. For instance, RAD51 cannot bypass short regions of heterology (43). Though heterology bypass by RecA depends on ATP hydrolysis and therefore a dynamic filament, even where ATP hydrolysis is active, the average length of RAD51 patches, and the resulting joint molecules, would be too short to stabilize longer stretches of mis-paired bases. The arrangement of RAD51 as interrupted filaments is less prone than RecA to inhibition of strand exchange due to topological constraints from non-productive pairing interactions requiring a stiff recombinase filament (44).

It is of interest to speculate about possible mechanistic advantages of the RAD51-DNA filament arrangement we have obtained. Because ssDNA is highly flexible, the bare DNA gaps likely will act as hinges, creating a quite flexible RAD51-DNA structure. A stiff continuous nucleoprotein filament where association with the target only occurs at the filament ends allows only a single functional interaction point. The overall flexibility and dynamics of the RAD51 structure will promote multiple sites for potentially functional interactions between the filament segments and the target dsDNA. Thus a flexible filament could be an advantage in identifying homology because one diffusion-limited encounter would sample multiple regions of the target dsDNA. This advantage in homology search may not be evident in strand exchange assays because they do not report on homology search but rather detect the products of strand exchange, which may still be hindered by filament interruptions. The tracks of bare ssDNA in between RAD51 patches can also act as swivels to release topological constraints during joint-molecule formation, which is not possible for long continuous nucleoprotein filaments (44).

SUPPLEMENTARY DATA

Supplementary Data are available at NAR Online.

ACKNOWLEDGEMENTS

We thank Peter Veenhuizen for technical assistance. This work was supported by grants from the 'Stichting voor Fundamenteel Onderzoek der Materie (FOM)', which is financially supported by the 'Nederlandse Organisatie voor Wetenschappelijk Onderzoek (NWO)', the Association for International Cancer Research (AICR), and the European Commission (IP 512113). Funding to pay the Open Access publication charges for this article was provided by Nederlandse Organisatie voor Wetenschappelijk Onderzoek (NWO).

Conflict of interest statement. None declared.

REFERENCES

1. West,S.C. (2003) Molecular views of recombination proteins and their control. *Nat. Rev. Mol. Cell Biol.*, **4**, 435–445.
2. Wyman,C. and Kanaar,R. (2004) Homologous recombination: Down to the wire. *Curr. Biol*, **14**, R629–R631.
3. Conway,A.B., Lynch,T.W., Zhang,Y., Fortin,G.S., Fung,C.W., Symington,L.S. and Rice,P.A. (2004) Crystal structure of a Rad51 filament. *Nat. Struct. Mol. Biol.*, **11**, 791–796.
4. Yu,X., Jacobs,S.A., West,S.C., Ogawa,T. and Egelman,E.H. (2001) Domain structure and dynamics in the helical filaments formed by RecA and Rad51 on DNA. *Proc. Natl Acad. Sci. USA*, **98**, 8419–8424.S
5. Yu,X., VanLoock,M.S., Yang,S., Reese,J.T. and Egelman,E.H. (2004) What is the structure of the RecA-DNA filament? *Curr. Protein Pept. Sc.*, **5**, 73–79.
6. Ristic,D., Modesti,M., van der Heijden,T., van Noort,J., Dekker,C., Kanaar,R. and Wyman,C. (2005) Human Rad51 filaments on double- and single-stranded DNA: Correlating regular and irregular forms with recombination function. *Nucleic Acids Res.*, **33**, 3292–3302.
7. VanLoock,M.S., Yu,X., Yang,S.X., Lai,A.L., Low,C., Campbell,M.J. and Egelman,E.H. (2003) ATP-Mediated conformational changes in the RecA filament. *Structure*, **11**, 187–196.
8. Ogawa,T., Yu,X., Shinohara,A. and Egelman,E.H. (1993) Similarity of the yeast Rad51 filament to the bacterial RecA filament. *Science*, **259**, 1896–1899.
9. Benson,F.E., Stasiak,A. and West,S.C. (1994) Purification and characterization of the human Rad51 protein, an analog of *Escherichia coli* RecA. *EMBO J.*, **13**, 5764–5771.
10. Sung,P. and Robberson,D.L. (1995) DNA strand exchange mediated by a Rad51-ssdna nucleoprotein filament with polarity opposite to that of RecA. *Cell*, **82**, 453–461.
11. van der Heijden,T., van Noort,J., van Leest,H., Kanaar,R., Wyman,C., Dekker,N. and Dekker,C. (2005) Torque-limited RecA polymerization on dsDNA. *Nucleic Acids Res.*, **33**, 2099–2105.
12. Shivashankar,G.V., Feingold,M., Krichevsky,O. and Libchaber,A. (1999) RecA polymerization on double-stranded DNA by using single-molecule manipulation: The role of ATP hydrolysis. *Proc. Natl Acad. Sci. USA*, **96**, 7916–7921.
13. Roca,A.I. and Cox,M.M. (1997) RecA protein: Structure, function, and role in recombinational DNA repair. *Prog. Nucleic Acid Res. Mol. Biol.*, **56**, 129–223.
14. Galletto,R., Amitani,I., Baskin,R.J. and Kowalczykowski,S.C. (2006) Direct observation of individual RecA filaments assembling on single DNA molecules. *Nature*, **443**, 875–878.
15. Joo,C., McKinney,S.A., Nakamura,M., Rasnik,I., Myong,S. and Ha,T. (2006) Real-time observation of RecA filament dynamics with single monomer resolution. *Cell*, **126**, 515–527.
16. Liu,Y.L., Stasiak,A.Z., Mcllwraith,M.J., Stasiak,A. and West,S.C. (2004) Conformational changes modulate the activity of human RAD51 protein. *J. Mol. Biol.*, **337**, 817–827.
17. De Zutter,S.K. and Knight,K.L. (1999) The hRad51 and RecA proteins show significant differences in cooperative binding to single-stranded DNA. *J. Mol. Biol.*, **293**, 769–780.
18. Bugreev,D.V. and Mazin,A.V. (2004) Ca^{2+} activates human homologous recombination protein Rad51 by modulating its ATPase activity. *Proc. Natl Acad. Sci. USA*, **101**, 9988–9993.
19. Strick,T.R., Allemand,J.F., Bensimon,D. and Croquette,V. (1998) Behavior of supercoiled DNA. *Biophys. J.*, **74**, 2016–2028.
20. van Noort,J., Verbrugge,S., Goosen,N., Dekker,C. and Dame,R.T. (2004) Dual architectural roles of HU: Formation of flexible hinges and rigid filaments. *Proc. Natl Acad. Sci. USA*, **101**, 6969–6974.
21. Turner,M.S. (2000) Two time constants for the binding of proteins to DNA from micromechanical data. *Biophys. J.*, **78**, 600–607.
22. Marko,J.F. and Siggia,E.D. (1995) Stretching DNA. *Macromolecules*, **28**, 8759–8770.
23. Yang,S.X., VanLoock,M.S., Yu,X. and Egelman,E.H. (2001) Comparison of bacteriophage T4 UvsX and human Rad51 filaments suggests that RecA-like polymers may have evolved independently. *J. Mol. Biol.*, **312**, 999–1009.
24. Chi,P., Van Komen,S., Sehorn,M.G., Sigurdsson,S. and Sung,P. (2006) Roles of ATP binding and ATP hydrolysis in human Rad51 recombinase function. *DNA Repair*, **5**, 381–391.
25. Namsaraev,E.A. and Berg,P. (1998) Binding of Rad51p to DNA – interaction of Rad5lp with single- and double-stranded DNA. *J. Biol. Chem.*, **273**, 6177–6182.
26. Weiss,J.N. (1997) The Hill equation revisited: uses and misuses. *FASEB J.*, **11**, 835–841.
27. Modesti,M., Ristic,D., van der Heijden,T., Dekker,C., van Mameren,J., Peterman,E.J.G., Wuite,G.J.L., Kanaar,R. and Wyman,C. (2007) Fluorescent human RAD51 reveals multiple nucleation sites and filaments segments tightly associated along a single DNA molecule. *Structure*, **15**, 599–609.
28. Tombline,G., Shim,K.S. and Fishel,R. (2002) Biochemical characterization of the human RAD51 protein - II. Adenosine nucleotide binding and competition. *J. Biol. Chem.*, **277**, 14426–14433.
29. Bouchiat,C., Wang,M.D., Allemand,J.F., Strick,T., Block,S.M. and Croquette,V. (1999) Estimating the persistence length of a worm-like chain molecule from force-extension measurements. *Biophys. J.*, **76**, 409–413.

30. Hegner,M., Smith,S.B. and Bustamante,C. (1999) Polymerization and mechanical properties of single RecA-DNA filaments. *Proc. Natl Acad. Sci. USA*, **96**, 10109–10114.
31. van Mameren,J., Modesti,M., Kanaar,R., Wyman,C., Wuite,G.J.L. and Peterman,E.J.G. (2006) Dissecting elastic heterogeneity along DNA molecules coated partly with Rad51 using concurrent fluorescence microscopy and optical tweezers. *Biophys. J.*, **91**, L78–L80.
32. Granéli,A., Yeykal,C.C., Robertson,R.B. and Greene,E.C. (2006) Long-distance lateral diffusion of human Rad51 on double-stranded DNA. *Proc. Natl Acad. Sci. USA*, **103**, 1221–1226.
33. McIlwraith,M.J., Van Dyck,E., Masson,J.Y., Stasiak,A.Z., Stasiak,A. and West,S.C. (2000) Reconstitution of the strand invasion step of double-strand break repair using human Rad51 Rad52 and RPA proteins. *J. Mol. Biol.*, **304**, 151–164.
34. Baumann,P., Benson,F.E., Hajibagheri,N. and West,S.C. (1997) Purification of human Rad51 protein by selective spermidine precipitation. *Mutat. Res. DNA Repair*, **384**, 65–72.
35. Tombline,G., Heinen,C.D., Shim,K.S. and Fishel,R. (2002) Biochemical characterization of the human RAD51 protein - III. – Modulation of DNA binding by adenosine nucleotides. *J. Biol. Chem.*, **277**, 14434–14442.
36. Shin,D.S., Pellegrini,L., Daniels,D.S., Yelent,B., Craig,L., Bates,D., Yu,D.S., Shivji,M.K., Hitomi, and C.., (2003) Full-length archaeal Rad51 structure and mutants: mechanisms for RAD51 assembly and control by BRCA2. *EMBO J.*, **22**, 4566–4576.
37. Wyman,C. and Kanaar,R. (2006) DNA double-strand break repair: All's well that ends well. *Annu. Rev. Genet.*, **40**, 363–383.
38. Esashi,F., Galkin,V.E., Yu,X., Egelman,E.H. and West,S.C. (2007) Stabilization of RAD51 nucleoprotein filaments by the C-terminal region of BRCA2. *Nat. Struct. Mol. Biol.*, **14**, 468–474.
39. Davies,O.R. and Pellegrini,L. (2007) Interaction with the BRCA2 C terminus protects RAD51-DNA filaments from disassembly by BRC repeats. *Nat. Struct. Mol. Biol.*, **14**, 475–483.
40. Petalcorin,M.I., Galkin,V.E., Yu,X., Egelman,E.H. and Boulton,S.J. (2007) Stabilization of RAD-51-DNA filaments via an interaction domain in Caenorhabditis elegans BRCA2. *Proc. Natl Acad. Sci. USA*, **104**, 8299–8304.
41. Shivji,M.K.K. and Venkitaraman,A.R. (2004) DNA recombination, chromosomal stability and carcinogenesis: insights into the role of BRCA2. *DNA Repair*, **3**, 835–843.
42. Symington,L.S. and Heyer,W.D. (2006) Some disassembly required: role of DNA translocases in the disruption of recombination intermediates and dead-end complexes. *Genes Dev.*, **20**, 2479–2486.
43. Holmes,V.F., Benjamin,K.R., Crisona,N.J. and Cozzarelli,N.R. (2001) Bypass of heterology during strand transfer by Saccharomyces cerevisiae Rad51 protein. *Nucleic Acids Res.*, **29**, 5052–5057.
44. Lusetti,S.L. and Cox,M.M. (2002) The bacterial RecA protein and the recombinational DNA repair of stalled replication forks. *Annu. Rev. Biochem.*, **71**, 71–100.
45. Dessinges,M.N., Maier,B., Zhang,Y., Peliti,M., Bensimon,D. and Croquette,V. (2002) Stretching single stranded DNA, a model polyelectrolyte. *Phys. Rev. Lett.*, **89**, 248102.